COMMUNICATION

Check for updates

Assessing the role of plasma-engineered acceptor-like intra- and inter-grain boundaries of heterogeneous WS₂–WO₃ nanosheets for photocurrent characteristics†

Gopika Gopakumar, Shantikumar V. Nair and Mariyappan Shanmugam [ID] *

High-temperature annealing in tungsten disulfide resulted in heterogeneous WS₂–WO₃ in which intra- (within WS₂ and WO₃) and inter- (between WS₂ and WO₃) grain boundaries were observed, which were highly critical for charge transport and recombination. The heterogeneous WS₂–WO₃ phase was evidenced by observing the coexistence of *d*-spacing values of 0.26 nm (WS₂) and 0.37 nm (WO₃) in transmission electron microscopic (TEM) studies. Further systematic high-resolution TEM studies elucidated that intra-grain boundaries separated crystallites within WS₂ and WO₃, while inter-grain boundaries separated WS₂ from WO₃. As WS₂ and WO₃ are both n-type, these defects are acceptor-like in the grain boundaries and they actively participate in the capture (trapping) process, which impedes charge transport characteristics in the heterogeneous WS₂–WO₃ films. Plasma treatment in the heterogeneous WS₂–WO₃ film, for 60 minutes using argon, energetically modulated the defects in the intra/inter-grain boundaries, as evidenced from detailed comparative photocurrent characteristics obtained individually in (i) pristine WS₂, (ii) heterogeneous WS₂–WO₃ and (iii) Ar plasma-treated heterogeneous WS₂–WO₃ films under blue and green lasers, along with AM1.5 (1 sun) illumination. Detrimental roles (trapping/de-trapping and scattering) of grain boundary states on photoelectrons were seen to be significantly suppressed under the influence of plasma.

Introduction

Graphene, with its two-dimensional (2D) layered structure, has been a wonder material, breaking technical limits on the applications of conventional functional materials in nano-electronics, with new boundaries with exceptional structural, electrical and mechanical characteristics being established.[1–3] The arrival of graphene into optoelectronic applications has opened up a highly challenging new technological era, in which

Amrita Centre for Nanosciences and Molecular Medicine, Amrita Vishwa Vidyapeetham, Kerala-682041, India. E-mail: mshanmugam@aims.amrita.edu

† Electronic supplementary information (ESI) available. See DOI: 10.1039/d0na00158a

multifarious 2D layered categories of semiconductors, metals and dielectrics have been explored.[4–6] Tungsten disulfide (WS₂) has been identified as a potential 2D-layered semiconductor, exhibiting a hexagonal honeycomb lattice structure, with a tunable optical band gap in the range of direct 1.8 eV (monolayer) to indirect 1.3 eV (bulk).[7–10] Wet chemical methods, chemical vapor deposition (CVD) and micro-mechanical/chemical exfoliation techniques are well-known methods reported for the synthesis of WS₂.[11–15] It has been observed that exfoliation and CVD-based approaches yield good-quality WS₂ with the possibility of precise control over the thickness (number of atomic layers).[16,17] Recently, atomic layer deposition-based, atomically thin wafer-scale production of WS₂ has been demonstrated, which allows the possibility of building large-area electronic networks based on nanofabrication.[18–20]

In general, high-temperature processes or any other special treatment methods, such as UV–ozone, on WS₂ cause dominant oxidation, resulting in the oxide phase coexisting in the same material along with the parent sulfide component.[21] Photo-oxidation due to ambient light exposure for a week in WS₂ films led to oxidation, specifically under excitation energies above the trion excitation energy.[22] It has been observed that WS₂ is highly stable below 350 °C but becomes sensitive at temperatures above 450 °C, at which WS₂ is transformed into WO₃, with further increase in thermal treatment causing significant changes in morphology as well.[23] Photocatalytic activity in lateral heterostructures of WS₂/WO₃ has been reported and the study showed the possibility of achieving simultaneous interaction of oxygen with both sides in WS₂ *via* selective oxidation.[24] The kinetics of the hydrogen evolution reaction were significantly improved using heterostructure hybrid catalysts based on WS₂/WO₃.[25] It has recently been demonstrated, *via* the *in situ* anodic oxidation of a WS₂ film, that a current density of 100 mA cm⁻² at 152 mV was attributable to the excellent kinetics of the hydrogen evolution reaction.[26] It has been observed that the presence of photocatalytic activity and photoresponsive behavior can be significantly improved by introducing WO₃ in WS₂, as the charge transport

characteristics are improved.[27] Azam *et al.* have reported electrochromic devices based on 2D WO_3 obtained from the oxidation of 2D WS_2 that showed 62.57% color modulation at a wavelength of 700 nm, which has been claimed to be approximately three times more than for bulk WO_3.[28] Recently, photovoltaic application of WS_2 processed from WO_3 was demonstrated as a counter electrode material resulting in 7.2% photoconversion efficiency.[29] Our previous study demonstrated the photovoltaic effect in dye-sensitized 2D-layered WS_2 films, which showed the coexistence of WS_2 and WO_3.[30]

In this work, a detailed structural, optical, and nano-morphological evolution of heterogeneous WS_2–WO_3 films is studied and their influences on photocurrent measurements performed under three different illuminations are presented. Charge transport characteristics in the heterogeneous WS_2–WO_3 films under dark and three different illuminations are explained in terms of the presence of the oxy-sulfide heterogeneous phase WS_2–WO_3, the two types of grain boundaries separating them and the associated defects within the boundaries. Finally, the effect of argon plasma interaction with WS_2–WO_3 films, and its consequences, are explained.

Experimental section

Pristine WS_2 powder (99% purity, Alfa Aesar) was used to prepare a colloidal paste by mixing it with a polyester (99% purity, Sigma Aldrich) polymer solution. The colloidal paste was then doctor-bladed onto glass substrates (Corning) and annealed at 530 °C for 1 h. After the annealing process, the samples were allowed to cool to room temperature with no external influences. A crack-free, uniform WS_2 thin-film coating was achieved, as illustrated in Fig. 1(a). The sample was further

thermally treated and a significant change in color was observed representing WS_2–WO_3, as shown in Fig. 1(a). The sample was then subjected to argon (Ar) plasma for 60 minutes with a radiofrequency power of 10 W and a gas flow rate of 30 sccm. The plasma-treated sample is also shown at the bottom in Fig. 1(a).

Photocurrent measurements were performed on all three samples: (i) pristine WS_2, (ii) heterogeneous WS_2–WO_3 and (iii) Ar plasma-treated heterogeneous WS_2–WO_3, by coating aluminum metal contacts using DC sputtering with a power of 50 W and Ar gas flow rate of 30 sccm. The aluminum electrode deposition was carried out for 30 minutes on the three samples, with a gap of 2 mm maintained by a shadow mask. The aluminum electrode-coated WS_2, WS_2–WO_3 and plasma-processed WS_2–WO_3 devices are shown in Fig. 1(b). Fig. 1(c) shows a schematic illustration of the coexistence of WS_2–WO_3 in the samples illustrated in Fig. 1(a). The samples were then illuminated using three different light sources: (i) white light with AM1.5 photon flux, (ii) blue (405 nm) and (iii) green (532 nm) lasers to measure the current–voltage (*I*–*V*) characteristics, as shown in Fig. 1(d). Pristine WS_2, WS_2–WO_3 and plasma-processed WS_2–WO_3 were used as charge transport channels along with aluminum metal contacts to inject/collect the charge carriers, like a source/drain.

Results and discussion

Fig. 2(a) shows the X-ray diffraction (XRD) patterns corresponding to pristine WS_2, WS_2–WO_3 and plasma-processed WS_2–WO_3 films. The pristine WS_2 showed peaks at 2θ values of 14.4°, 28.9°, 33.5°, 33.6°, 39.5°, 43.9° and 58.3°, corresponding to the indices (002), (004), (100), (101) (103), (006) and
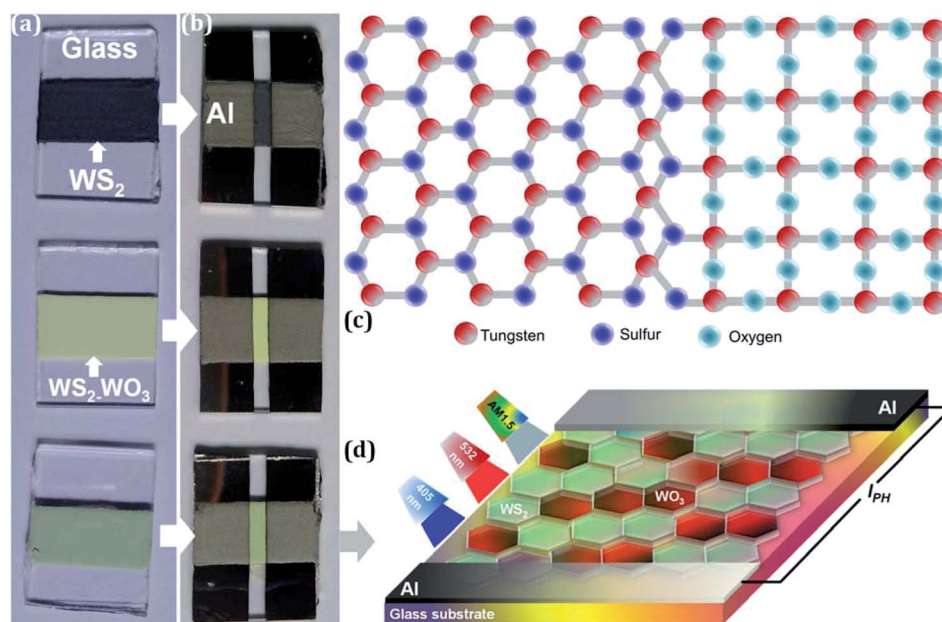

Fig. 1 (a) Digital images of pristine WS_2, heterogeneous WS_2–WO_3, and plasma-processed heterogeneous WS_2–WO_3. (b) Corresponding fabricated devices using Al as metal contacts. (c) Schematic illustration showing the coexistence of WS_2 and WO_3 in the crystal structure, giving heterogeneity. (d) Schematic of the fabricated two-terminal devices using heterogeneous WS_2–WO_3 as a photoactive material.
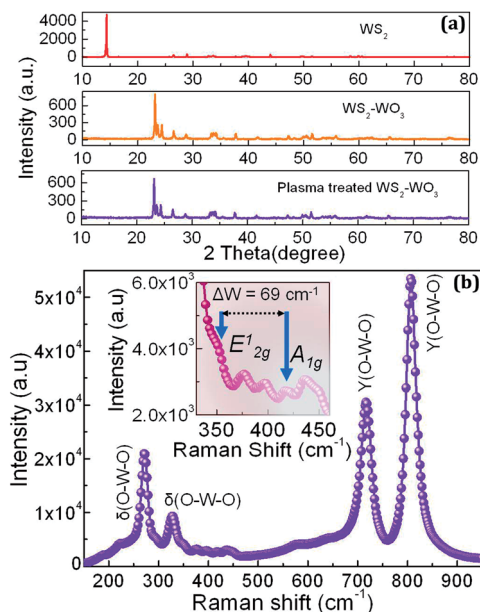
Fig. 2 (a) XRD patterns obtained from pristine WS$_2$, WS$_2$–WO$_3$ and plasma-treated WS$_2$–WO$_3$ films. (b) Raman spectrum obtained from the plasma-treated WS$_2$–WO$_3$ film.

(110), respectively. These values were further matched with previously reported studies and it was observed that all were in good agreement.[31,32] All the XRD peaks evidenced the presence of crystalline WS$_2$, used as a source material for the preparation of the oxy-sulfide phase of WS$_2$.

The peak at 14.4° indexed to (002) represents the stacked crystalline layers in the bulk WS$_2$. The XRD pattern of the oxy-sulfide phase in WS$_2$ (represented as WS$_2$–WO$_3$) showed the absence of the 14.4° peak, confirming the transformation of pristine WS$_2$ into the mixed oxy-sulfide phase. In general, the XRD peak intensity is significantly affected by the exfoliation process, as the atomically thinner region is reached and the peak vanishes upon complete phase transformation, as evidenced from previously reported studies.[31,33] The other major peaks were observed at 23.1°, 23.6°, 24.3°, 33.6° and 34.1° corresponding to the planes (002), (020), (200), (022) and (201), respectively. These crystalline peaks represent the presence of monoclinic WO$_3$, as reported elsewhere.[34] Due to the relatively lower amount of WS$_2$ in WO$_3$, the characteristic XRD peaks of WS$_2$ were not observed. It has already been reported that the absence of peaks due to lower concentration, in terms of phase fraction, is relatively common in 2D-layered van der Waals materials.[35–37] The XRD pattern of the plasma-treated oxy-sulfide phase in WS$_2$ was observed to be very similar to the XRD pattern of WS$_2$–WO$_3$. This confirmed that plasma treatment did not change the crystallographic nature of the WS$_2$–WO$_3$. Moreover, it was also realized that the presence of the WS$_2$–WO$_3$ phase in WS$_2$ is highly stable, and could not be altered by the low power argon plasma used in the present study.

Fig. 2(b) shows the Raman-active modes observed in the plasma-processed WS$_2$–WO$_3$ sample. WO$_3$ exhibited high intensity modes compared with WS$_2$, which showed low intensity Raman modes. The bending vibrations belong the O–W–O bonds observed at 271.1 and 327.1 cm^{-1} are denoted as δ(O–W–O). The stretching of the O–W–O bonds observed at 716.7 and 806.6 cm^{-1} is represented as γ(O–W–O). Both bending and stretching vibrational modes are specific for the monoclinic WO$_3$ structure.[28,38,39] WS$_2$ exhibited in-plane A$_{1g}$ and out of plane E$^1_{2g}$ vibrational modes, as shown in the inset. E$^1_{2g}$ appeared as
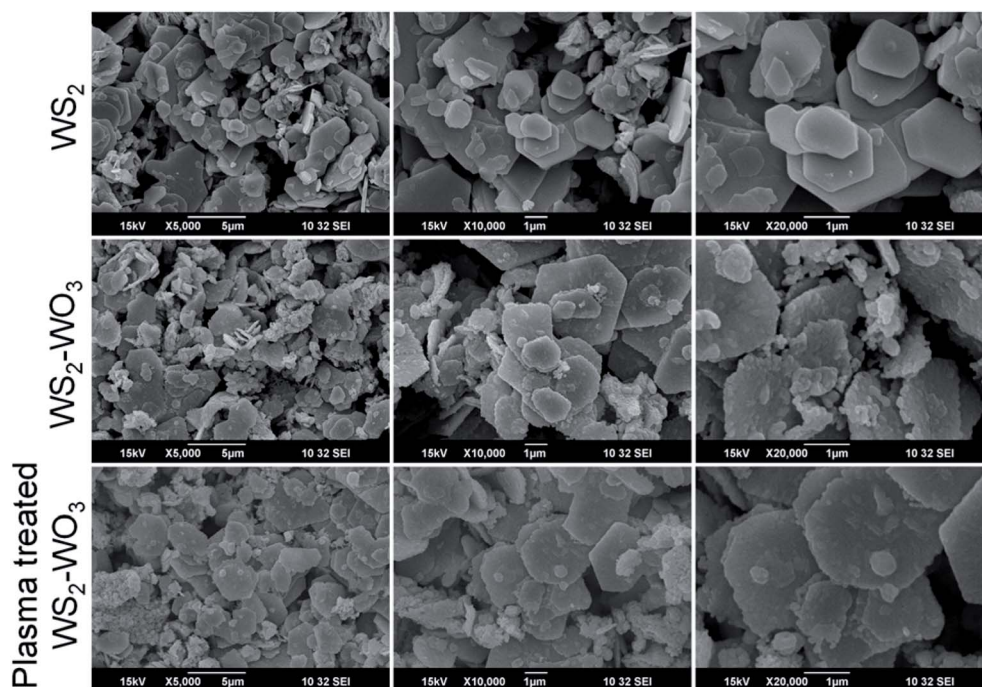

Fig. 3 Surface morphology of pristine WS$_2$ (row 1), heterogeneous WS$_2$–WO$_3$ (row 2) and plasma-treated WS$_2$–WO$_3$ (row 3).

a shoulder peak at the high intensity Raman mode of WO_3, as a result of which the difference in peak intensity between E_{2g}^1 and A_{1g} is not very clear. The frequency difference, Δw, between the two modes of WS_2 is directly related to its thickness. If Δw is 70 cm^{-1}, then it represents the bulk, and values less than this are considered to indicate the presence of a monolayer, bilayer and trilayer.[40] In the case of the WS_2 oxysulfide phase, Δw was found to be $\sim$69 cm^{-1}, indicating the presence of a few layers in WS_2. Atmospheric oxygen intercalated into the WS_2 sheets while undergoing high-temperature annealing and reacted with tungsten in the surface defects forming the oxy-sulfide phase in WS_2. The other Raman modes, shown in the inset at 376.8 and 435.9 cm^{-1}, represent vibrations due to $\gamma(W–OH_2)$ and $\delta(O–W–O)$ in WO_3 respectively. The $\gamma(W–OH_2)$ vibration could be due to water molecules present at the surface of the WO_3, as the characterization was carried out under atmospheric conditions.[41]

Fig. 3 shows three rows of scanning electron microscopy images obtained from pristine WS_2 (row 1), heterogeneous WS_2–WO_3 (row 2) and plasma-treated WS_2–WO_3 (row 3). The difference between the three columns is just in the magnification, as 5000$\times$, 10 000$\times$ and 20 000$\times$. All three films exhibited randomly distributed platelet structures. The platelets were micrometers in size with dominant hexagonal shapes, as can be seen from the 20 000$\times$ images (column 3). In the case of pristine WS_2 film, the hexagonal platelets were observed to be smooth with sharp edges. In the case of the heterogeneous WS_2–WO_3 film, the precise hexagonal feature in the platelets was altered. This effect was even more significant in the case of plasma-treated WS_2–WO_3 film, as can be seen from row 3. It is clear that argon plasma energetically diffused into the randomly distributed hexagonal platelets and altered the distribution and surface smoothness, as can be clearly seen at 20 000$\times$.

The high-resolution transmission electron microscopy (HR-TEM) images shown in Fig. 4(a)–(f) were used to analysis and explain the concepts of inter- and intra-grains along with boundaries. Fig. 4(a) shows a well-defined intra-grain boundary (within the same phase) in WO_3, as confirmed *via* the *d*-spacing of 0.37 nm. The grain boundary that separates the two grains in WO_3 is marked with yellow dotted lines. Fig. 4(b) illustrates the inter-grain boundaries (between different phases) separating the WS_2 from WO_3, as evidenced by the *d*-spacing values of 0.26 and 0.37 nm, respectively.

Plasma treatment in the heterogeneous WS_2–WO_3 film showed that the boundaries were sharpened, with not much spread into the grains, as shown in Fig. 4(c) and (d). This can be attributed to the plasma energy facilitating increased grain size distribution, which eventually reduced the grain boundaries. Fig. 4(c) shows the plasma-treated intra-grain boundary separating two WO_3 grains, but the boundary is observed to be sharper compared with the sample without plasma treatment. Fig. 4(d) shows the plasma-treated intra-grain boundary corresponding to WS_2 grains, as confirmed by the *d*-spacing of 0.26 nm. Fig. 4(e) and (f) depict the inter-grain boundaries isolating WS_2 and WO_3 very precisely. Fast-Fourier transform
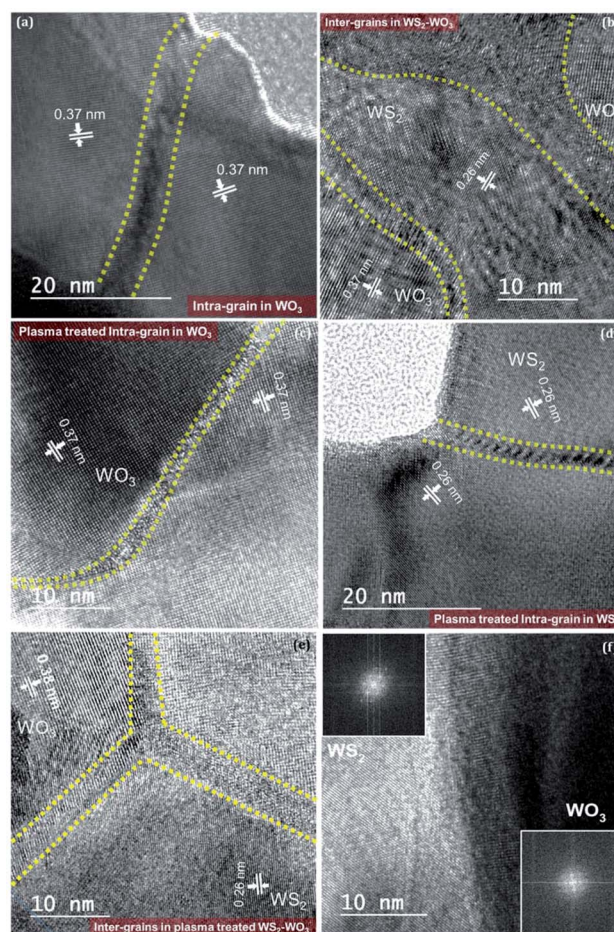
Fig. 4 HR-TEM images showing the evolution of (a) intra-grain boundary in WO_3, (b) inter-grain boundary in WS_2–WO_3, (c) intra-grain boundary in WO_3 after plasma treatment, (d) intra-grain boundary in WS_2 after plasma treatment, (e) inter-grain boundary in WS_2–WO_3 after plasma treatment and (f) FFT shows the presence of inter-grain boundary separating WS_2 and WO_3.

analysis further verified the presence of an inter-grain boundary separating WS_2 and WO_3 abruptly, as shown in Fig. 4(f).

Fig. 5 shows the UV-visible absorbance spectra of the WS_2 oxy-sulfide phase with and without plasma treatment in the
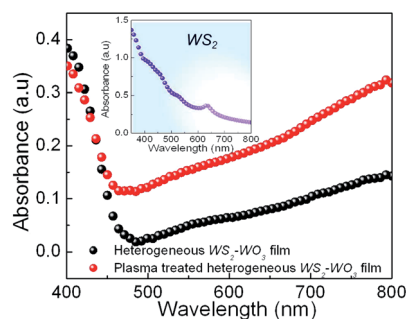
Fig. 5 UV-visible optical absorbance spectra of heterogeneous WS_2–WO_3 film before and after plasma treatment, with the inset showing the absorbance of pristine WS_2 film.

wavelength range 350–800 nm. The inset shows the absorbance spectrum of exfoliated WS_2 sheets. The absorbance spectra of the oxy-sulfide phase of WS_2 showed a broad absorbance due to the coexistence of WO_3 and WS_2 in the sample. WO_3, with a band gap of 2.7 eV, showed some photo-absorption in the visible spectrum, which is consistent with previous studies.[42,43] Optical absorbance of WS_2 is highly tunable and is sensitive to many factors, such as number of layers,[44] defects,[45–47] and strain.[48,49] Defects in 2D-layered materials play a critical role in optical absorbance.[46] In the case of the oxy-sulfide phase of WS_2, the synthesis creates many defects associated with sulfur and oxygen. In addition, the presence of grains and grain

boundaries also creates many defects, which affect the band gap of WS_2.[45–47]

Fig. 6 shows comparative I–V characteristics of (i) pristine WS_2, (ii) heterogeneous WS_2–WO_3 and (iii) plasma-treated WS_2–WO_3 films. The measured I–V characteristics for all three samples were highly linear in an applied bias region of ±10 V. This first shows that all three samples formed a highly ohmic junction with aluminum contacts, which facilitated efficient charge transport through pristine WS_2, heterogeneous WS_2–WO_3 and plasma-treated WS_2–WO_3 films. Fig. 6(a)–(d) specifically represents I–V characteristics obtained in the dark and under blue laser, green laser and AM1.5 illumination, respectively. The insets in all four categories represent just an
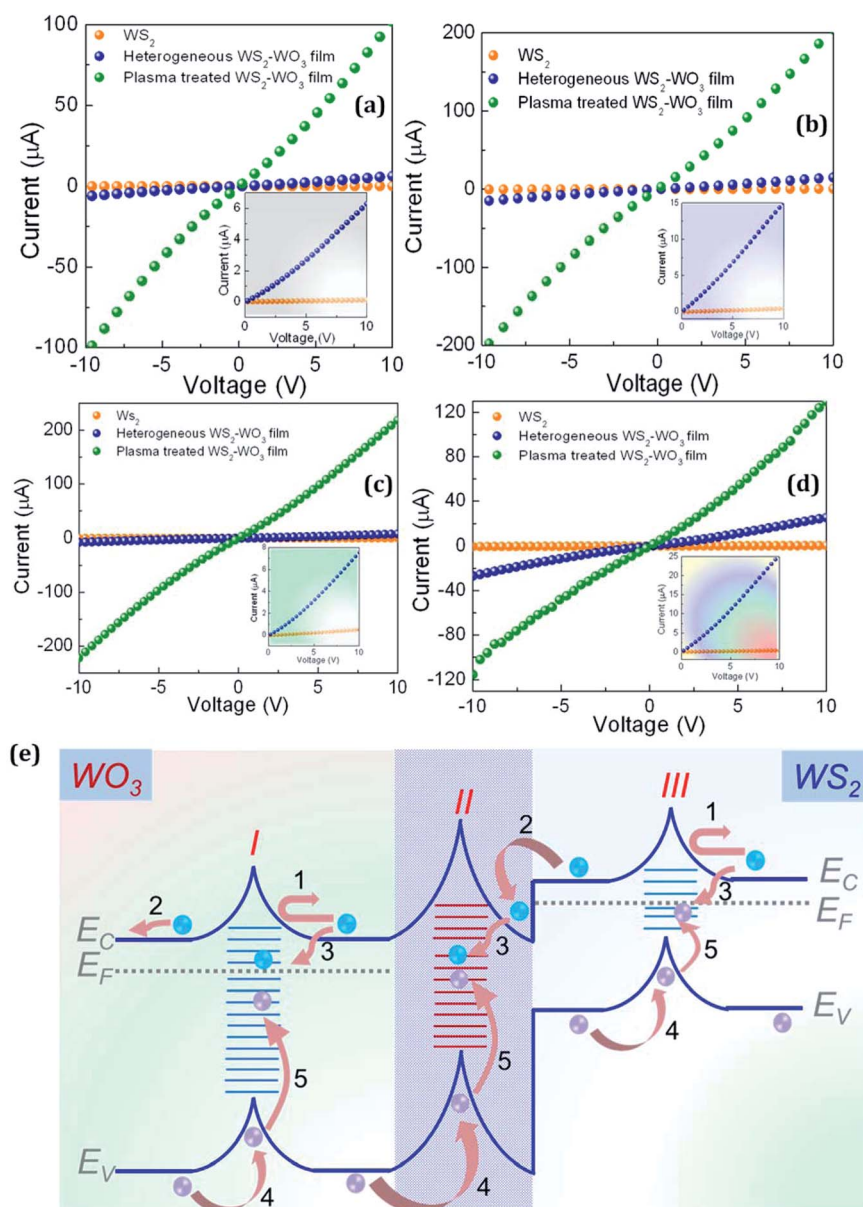

Fig. 6 I–V characteristics of the pristine WS_2, heterogeneous WS_2–WO_3 and plasma-treated WS_2–WO_3 measured under (a) dark, (b) blue laser illumination, (c) green laser illumination and (d) AM1.5 illumination. (e) Schematic illustration showing the presence of the inter-grain boundary between WS_2–WO_3 and the intra-grain boundary in WS_2 and WO_3 on potential distribution, with various physical processes interfering with charge transport and recombination dynamics.

expanded view of the WS$_2$ and heterogeneous WS$_2$–WO$_3$ samples in an applied bias region of 0–10 V, as these were very close to each other and lower in comparison with the plasma-treated sample. Fig. 6(e) shows the energy band alignment in the heterogeneous WS$_2$–WO$_3$ films. Three potential barriers are illustrated as I, II and III. Barrier I situated in WO$_3$ represents a potential disruption energy band structure within WO$_3$. When multiple grains form together to make a thin film, it is obvious that grain boundaries are established within the phase and such boundaries can be considered as intra-grain boundaries. Similarly, the grain boundary within WS$_2$ grains is represented in region III, with a possible interruption in the potential profile as illustrated. Interestingly, when two different phases coexist to form a heterogeneous material system, an inter-grain boundary is also established. The inter-grain boundaries create a potential barrier for charge transport at the interface of WS$_2$/WO$_3$. In general, defect-free single crystalline semiconductors are expected not to show such disorders in their energetics, but it is quite impossible to meet such criteria in a real case, as material synthesis and device fabrication processes involve several experimental difficulties that directly cause disorder in materials. In this case, both WS$_2$ and WO$_3$ are both n-type materials existing together and forming the heterogeneity with well-defined inter-grain boundaries. Grain boundaries, in general, possess lot of crystallographic defects, as the structural disorder predominantly occurs right at the interface between WS$_2$ and WO$_3$, as shown in region II in Fig. 6(e).

Charge transport and recombination dynamics in the heterogeneous WS$_2$–WO$_3$ are illustrated through the various processes listed (1)–(5). Optical excitation in WS$_2$ generates a free electron and hole in conduction (E_C) and valence (E_V) band edges, respectively; processes (1). The free electron in the E_C should move towards the E_C of WO$_3$ to stabilize, due to the position of the E_C of WO$_3$, which is a few meV below WS$_2$. However, it has to pass through the structurally disordered region II, the inter-grain boundary, which separates WS$_2$ from WO$_3$ via defect distribution as illustrated.

Grain boundaries are considered to be charged by majority carriers, in this case electrons, and to affect the band structure by creating potential barriers, as illustrated. Charge transport is impeded by such a potential barrier, as shown in process (2). Thus, photogenerated electrons can be trapped, process (3), in such defect states and attain localized distribution, which can effectively attract a hole from E_V, as illustrated in processes (4) and (5). In general, the presence of defects in grain boundaries facilitates bringing photogenerated electrons and holes together (electron–hole capture) in the nanoscale range, at which point recombination becomes prominent. In this situation the defects in inter- and intra-grain boundaries act as acceptor-like states, which actively participate in electron capture, making them negatively charged. The negatively charged defects cause hole transport in the E_V and eventually both electron and hole transport processes are affected. Plasma is an energetic environment, which can interact with functional materials to engineer structural and optoelectronic properties. This energetic environment is capable of passivating defects in the grain boundaries of materials and thus reduces their

capability and probability for charge trapping. It also reduces the potential barriers in the intra- and inter-grain boundaries that were established due to the presence of defects. This influences the electron–hole capture in the trap states and effectively improves charge transport kinetics. The change in currents measured under different situations evidences the fact that defects at the grain boundaries and their activity on charge transport characteristics are controlled by plasma treatment.

Fig. 7(a) shows the photoresponsivity (current due to the exciton generation via light exposure) of the pristine WS$_2$, heterogeneous WS$_2$–WO$_3$ and plasma-treated WS$_2$–WO$_3$ films. In order to represent a comparative plot for the photoresponsive characteristics of the three samples, an applied bias of 10 V was used. The increment in current values (δI) for pristine WS$_2$, heterogeneous WS$_2$–WO$_3$ and plasma-treated WS$_2$–WO$_3$ films was calculated under AM1.5 photon flux, blue and green laser illuminations with respect to the current values measured under dark condition: as $I_{Effective} = I_{Illumination} - I_{Dark}$, where $I_{Effective}$ represents the photoresponsivity of the specific sample. In Fig. 7(a), the photoresponsivity of pristine WS$_2$ was found to be very minimal under AM1.5 (0.30 µA) and blue laser (0.32 µA) illuminations, with a slight increase under green laser (0.41 µA) illumination. This is due to the bulk nature, since the WS$_2$ layers were almost stacked while coating the films. The photoresponsivity values of the heterogeneous WS$_2$–WO$_3$ were found to be reduced in the case of blue (8.7 µA) and green (1.3 µA) laser illumination at an applied bias of 10 V, when compared with
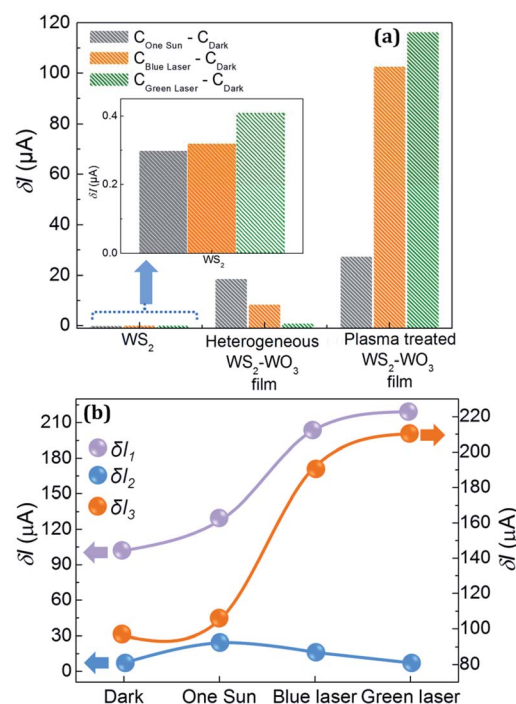

Fig. 7 (a) Photoresponsivity of pristine WS$_2$, heterogeneous WS$_2$–WO$_3$ and plasma-treated WS$_2$–WO$_3$ films at an applied bias of 10 V. (b) δI_1 and δI_2: increment in currents in heterogeneous WS$_2$–WO$_3$ and plasma-treated WS$_2$–WO$_3$ with respect to pristine WS$_2$. δI_3: increment in current of plasma-treated WS$_2$–WO$_3$ with respect to heterogeneous WS$_2$–WO$_3$.

AM1.5 illumination (19.0 µA). This can be attributed to more active recombination sites in the material, due to the presence of defects. The photoresponsivity under green laser was reduced due to the presence of defects in the intra-grain boundaries in WS_2 and WO_3 and inter-grain boundaries between WS_2 and WO_3. After plasma treatment the effects of grain boundary defects on charge transport characteristics are minimized, which can be seen from the bar graph for plasma-treated WS_2–WO_3 film. The photoresponsivity under the green laser (116.7 µA) was enhanced most when compared to values under the blue laser (102.9 µA) and AM1.5 illumination (27.7 µA). All of these results showed the possibility of engineering grain boundary defects in heterogeneous WS_2–WO_3.

Fig. 7(b) shows the increase in current values measured in the pristine WS_2, heterogeneous WS_2–WO_3 and plasma-treated WS_2–WO_3 films. The difference in current depicted for all three samples and all three illuminations under dark conditions are taken with the applied bias value of 10 V. In Fig. 7(b), δI_1 and δI_2 represent the increment in current in the case of heterogeneous WS_2–WO_3 and plasma-treated WS_2–WO_3 with respect to pristine WS_2. δI_3 represents the increase in the current of plasma-treated WS_2–WO_3 with respect to heterogeneous WS_2–WO_3. The arrows indicate the respective axes at which the change in current values was recorded. The δI_1 values were 24.9 µA under one sun illumination, 14.6 µA under blue laser, and 7.0 µA under green laser illumination, along with 6.2 µA under dark conditions. This shows that the increase in the current occurred after formation of the heterogeneous WS_2–WO_3 phase in the pristine WS_2. The increment in current values varied depending on the illumination conditions and sensitivity of the response of the material to incident energy. The δI_2 values were 129.1 µA under one sun illumination, 204.2 µA under blue and 217.9 µA under green laser illumination, along with 101.6 µA under dark conditions. This shows that there was an increment in current, even more than δI_1, after plasma treatment in the heterogeneous WS_2–WO_3 film. As in the case of δI_1, the values of δI_2 also varied depending on the illumination conditions and sensitivity of the photoresponse of the material. Contrary to δI_1, values of δI_2 showed a greater increase under blue and green lasers than under AM1.5 illumination. This can be attributed to the effective passivation of defect states associated with inter- and intra-grain boundaries by argon plasma treatment. Blue laser illumination is more interactive with the wide band gap of WO_3, while interaction of photons from the green laser is more effective with WS_2. Furthermore, δI_3 represents the increment in current values of plasma-treated WS_2–WO_3 samples with respect to heterogeneous WS_2–WO_3. The δI_3 values were 104.1 µA under one sun illumination, 189.6 µA under blue and 210.9 µA under green laser illumination, along with 95.5 µA under dark conditions. These values also showed an enhancement with respect to plasma treatment, suggesting the effective interaction of plasma with defects. These results showed that the photoresponse of heterogeneous WS_2–WO_3 was better than that of pristine WS_2, and plasma treatment of heterogeneous WS_2–WO_3 could further improve the charge transport characteristics by achieving effective defect passivation.

Conclusion

It has been inferred that the presence of heterogeneity in functional semiconductors establishes grain boundaries within and between the heterointerfaces, through which charge transport occurs. Such electronically active boundaries, which influence charge transport at the nanoscale, can be engineered *via* energetically active plasma treatment. The plasma environment in heterogeneous semiconducting phases alters the optoelectronic characteristics, as evidenced by optical absorption and electrical transport studies, suggesting that it is highly suitable for defect engineering at the nanoscale level.

Conflicts of interest

On behalf of all contributing authors, the corresponding author declares that there is no conflict of interest.

Acknowledgements

References

1 A. K. Geim, *Science*, 2009, **324**, 1530–1534.
2 K. S. Novoselov, V. I. Fal, L. Colombo, P. R. Gellert, M. G. Schwab and K. Kim, *Nature*, 2012, **490**, 192.
3 A. C. Ferrari, F. Bonaccorso, V. Fal'Ko, K. S. Novoselov, S. Roche, P. Bøggild, S. Borini, F. H. Koppens, V. Palermo, N. Pugno and J. A. Garrido, *Nanoscale*, 2015, **7**, 4598–4810.
4 K. F. Mak and J. Shan, *Nat. Photonics*, 2016, **10**, 216.
5 S. Manzeli, D. Ovchinnikov, D. Pasquier, O. V. Yazyev and A. Kis, *Nat. Rev. Mater.*, 2017, **2**, 17033.
6 C. Li, Q. Cao, F. Wang, Y. Xiao, Y. Li, J. J. Delaunay and H. Zhu, *Chem. Soc. Rev.*, 2018, **47**, 4981–5037.
7 Z. He, Y. Sheng, Y. Rong, G. D. Lee, J. Li and J. H. Warner, *ACS Nano*, 2015, **9**, 2740–2748.
8 M. Samadi, N. Sarikhani, M. Zirak, H. Zhang, H. L. Zhang and A. Z. Moshfegh, *Nanoscale Horiz.*, 2018, **3**, 90–204.
9 D. Ovchinnikov, A. Allain, Y. S. Huang, D. Dumcenco and A. Kis, *ACS Nano*, 2014, **8**, 8174–8181.
10 W. Li, T. Wang, X. Dai, X. Wang, C. Zhai, Y. Ma and S. Chang, *Solid State Commun.*, 2016, **225**, 32–37.
11 A. Anto Jeffery, C. Nethravathi and M. Rajamathi, *J. Phys. Chem. C*, 2014, **118**, 1386–1396.
12 J. Yu, X. Hu, H. Li, X. Zhou and T. Zhai, *J. Mater. Chem. C*, 2018, **6**, 4627–4640.
13 H. Yan, J. Li, D. Liu, X. Jing, D. Wang and L. Meng, *CrystEngComm*, 2018, **20**, 2324–2330.
14 C. Lan, C. Li, Y. Yin and Y. Liu, *Nanoscale*, 2015, **7**, 5974–5980.
15 V. Štengl, J. Tolasz and D. Popelková, *RSC Adv.*, 2015, **5**, 89612–89620.
16 M. Bosi, *RSC Adv.*, 2015, **5**, 75500–75518.

17 A. Thangaraja, S. M. Shinde, G. Kalita and M. Tanemura, *Mater. Lett.*, 2015, **156**, 156–160.

18 B. Groven, M. Heyne, A. Nalin Mehta, H. Bender, T. Nuytten, J. Meersschaut, T. Conard, P. Verdonck, S. Van Elshocht, W. Vandervorst and S. De Gendt, *Chem. Mater.*, 2017, **29**, 2927–2938.

19 A. Delabie, M. Caymax, B. Groven, M. Heyne, K. Haesevoets, J. Meersschaut, T. Nuytten, H. Bender, T. Conard, P. Verdonck and S. Van Elshocht, *Chem. Commun.*, 2015, **51**, 15692–15695.

20 S. Yeo, D. K. Nandi, R. Rahul, T. H. Kim, B. Shong, Y. Jang, J. S. Bae, J. W. Han, S. H. Kim and H. Kim, *Appl. Surf. Sci.*, 2018, **459**, 596–605.

21 M. Kang, H. I. Yang and W. Choi, *J. Phys. D: Appl. Phys.*, 2019, **52**, 505105.

22 J. C. Kotsakidis, Q. Zhang, A. L. V. de Parga, M. Currie, K. Helmerson, D. K. Gaskill and M. S. Fuhrer, 2019, arXiv preprint arXiv:1906.00375.

23 H. K. Adigilli, B. Padya, L. Venkatesh, V. S. K. Chakravadhanula, A. K. Pandey and J. Joardar, *Phys. Chem. Chem. Phys.*, 2019, **21**, 25139–25147.

24 P. Zhou, Q. Xu, H. Li, Y. Wang, B. Yan, Y. Zhou, J. Chen, J. Zhang and K. Wang, *Angew. Chem., Int. Ed.*, 2015, **54**, 15226–15230.

25 X. Shang, Y. Rao, S. S. Lu, B. Dong, L. M. Zhang, X. H. Liu, X. Li, Y. R. Liu, Y. M. Chai and C. G. Liu, *Mater. Chem. Phys.*, 2017, **197**, 123–128.

26 L. Yang, X. Zhu, S. Xiong, X. Wu, Y. Shan and P. K. Chu, *ACS Appl. Mater. Interfaces*, 2016, **8**, 13966–13972.

27 N. Huo, Q. Yue, J. Yang, S. Yang and J. Li, *ChemPhysChem*, 2013, **14**, 4069–4073.

28 A. Azam, J. Kim, J. Park, T. G. Novak, A. P. Tiwari, S. H. Song, B. Kim and S. Jeon, *Nano Lett.*, 2018, **18**, 5646–5651.

29 S. H. Ahn and A. Manthiram, *Adv. Energy Mater.*, 2016, **6**, 1501814.

30 G. Gopakumar, S. V. Nair and M. Shanmugam, *Nanoscale*, 2020, **12**, 239–247.

31 Y. Hongjian, Y. Yong, L. Jianghao, M. Peiyan, W. Yucheng, Z. Fan and F. Zhengyi, *J. Mater. Chem. A*, 2015, **3**, 19439–19444.

32 M. A. Ibrahem, T. W. Lan, J. K. Huang, Y. Y. Chen, K. H. Wei, L. J. Li and C. W. Chu, *RSC Adv.*, 2013, **3**, 13193–13202.

33 W. H. Hu, G. Q. Han, F. N. Dai, Y. R. Liu, X. Shang, B. Dong, Y. M. Chai, Y. Q. Liu and C. G. Liu, *Int. J. Hydrogen Energy*, 2016, **41**, 294–299.

34 R. Ponnusamy, A. Gangan, B. Chakraborty and C. Sekhar Rout, *J. Appl. Phys.*, 2018, **123**, 024701.

35 Z. Chen, S. Liu, M. Q. Yang and Y. J. Xu, *ACS Appl. Mater. Interfaces*, 2013, **5**, 4309–4319.

36 Y. Min, G. He, Q. Xu and Y. Chen, *J. Mater. Chem. A*, 2014, **2**, 2578–2584.

37 W. C. Peng, X. Wang and X. Y. Li, *Nanoscale*, 2014, **6**, 8311–8317.

38 M. F. Daniel, B. Desbat, J. C. Lassegues, B. Gerand and M. Figlarz, *J. Solid State Chem.*, 1987, **67**, 235–247.

39 D. Mandal, P. Routh and A. K. Nandi, *Small*, 2018, **14**, 1702881.

40 H. Zeng, G. B. Liu, J. Dai, Y. Yan, B. Zhu, R. He, L. Xie, S. Xu, X. Chen, W. Yao and X. Cui, *Sci. Rep.*, 2013, **3**, 1608.

41 S. M. Kanan, Z. Lu, J. K. Cox, G. Bernhardt and C. P. Tripp, *Langmuir*, 2002, **18**, 1707–1712.

42 P. P. González-Borrero, F. Sato, A. N. Medina, M. L. Baesso, A. C. Bento, G. Baldissera, C. Persson, G. A. Niklasson, C. G. Granqvist and A. Ferreira da Silva, *Appl. Phys. Lett.*, 2010, **96**, 061909.

43 S. S. Kalanur, I. H. Yoo, K. Eom and H. Seo, *J. Catal.*, 2018, **357**, 127–137.

44 M. Zhou, Z. Zhang, K. Huang, Z. Shi, R. Xie and W. Yang, *Nanoscale*, 2016, **8**, 15262–15272.

45 S. Refaely-Abramson, D. Y. Qiu, S. G. Louie and J. B. Neaton, *Phys. Rev. Lett.*, 2018, **121**, 167402.

46 C. Kastl, R. J. Koch, C. T. Chen, J. Eichhorn, S. Ulstrup, A. Bostwick, C. Jozwiak, T. R. Kuykendall, N. J. Borys, F. M. Toma and S. Aloni, *ACS Nano*, 2019, **13**, 1284–1291.

47 H. Liu, C. Wang, D. Liu and J. Luo, *Nanoscale*, 2019, **11**, 7913–7920.

48 H. Song, X. Yu, M. Chen, M. Qiao, T. Wang, J. Zhang, Y. Liu, P. Liu and X. Wang, *Appl. Surf. Sci.*, 2018, **439**, 240–245.

49 R. Frisenda, M. Drüppel, R. Schmidt, S. M. de Vasconcellos, D. P. de Lara, R. Bratschitsch, M. Rohlfing and A. Castellanos-Gomez, *npj 2D Mater. Appl.*, 2017, **1**, 10.